

# Wall-modeled LES of three-dimensional intersecting shock wave/turbulent boundary-layer interactions

By L. Fu, S. T. Bose<sup>†</sup> AND P. Moin

## 1. Motivation and objectives

For both military and civil applications, vehicles flying at highly supersonic or hypersonic speed are promising candidates for future transportation (Leyva 2017). One principal challenge for designing such vehicles is the development of the thermal protection system (Candler 2019), which can withstand the immense thermal loading. The development of efficient and accurate simulation tools that can predict these aerodynamic characteristics, e.g., laminar-turbulent transition, flow separation, and heat transfer, can complement experimental campaigns (Schneider 2008; Sandham *et al.* 2014; Schuelein 2014; Willems *et al.* 2015). The use of simulation strategies would help reduce trial-and-error iterations expediting the design process (Gaitonde 2015), and provide additional data that would otherwise be difficult to probe or measure in experimental facilities.

Hypersonic wall-bounded flows for realistic flight vehicles can be characterized by high Reynolds numbers and cold surface temperatures compared to the free-stream stagnation temperature. The prohibitive computational costs associated with high Reynolds numbers are well known (Choi & Moin 2012), while the cold wall conditions exacerbate the near-wall resolution requirements associated with the large temperature gradients in the vicinity of peak viscous dissipation. As a result, direct numerical simulations (DNS) of these flows have been largely limited to simple geometries with low Reynolds numbers, e.g., high-speed compressible boundary layer flows (Duan *et al.* 2011), hypersonic boundary-layer transitional flow for a flared cone (Hader & Fasel 2019), turbulent boundary layer along a compression ramp (Adams 2000), and transitional shock/boundary layer interaction (Sandham *et al.* 2014).

In this work, the canonical model of a realistic inlet configuration of an air-breathing hypersonic vehicle is considered (Kussoy & Horstman 1992). The basic configuration consists of two sharp fins mounted on a flat plate. The salient flow features are characterized by a hypersonic turbulent boundary layer that approaches the two vertical fins, generating a crossing shock pattern as well as a separation zone with strong pressure gradient. The objective of the present work is to assess the accuracy of the wall modeled large-eddy simulation (WMLES) approach in the context of more complex geometries and complex flow regimes. In particular, emphasis is placed on the ability to predict surface heat fluxes and the complex separation pattern that arises due to the impinging shock structure.

The remainder of this work is organized as follows. In Section 2, the equilibrium wall model, as well as the employed numerical method, is briefly reviewed. In Section 3, the physical problem definition and the corresponding computational setup are discussed in

<sup>†</sup> Cascade Technologies Inc., Palo Alto.

detail. In Section 4, the numerical results are analyzed. The concluding remarks and discussions are given in Section 5.

## 2. Methodologies

### 2.1. Equilibrium wall model

For the near-wall region, resolving the near-wall turbulence structures directly, e.g., by wall-resolved LES, requires a computational cost similar to that of DNS and thus is not practical for high-Reynolds-number flows. Instead, in WMLES, the near-wall turbulence is modeled by a wall-stress-modeling strategy, and the outer layer is resolved by LES (Bose & Park 2018). Consequently, the dynamics of the entire inner boundary layer are not resolved and represented by the modeled wall shear stress,  $\tau_w$ , and heat flux,  $Q_w$ , supplied to the LES solution (Larsson *et al.* 2016).

Considering the equilibrium model for compressible flows, for which the convection and the pressure gradient terms are assumed to balance each other, the simplified momentum and total energy equations can be written as (Larsson *et al.* 2016)

$$\frac{d}{dy} \left[ (\mu + \mu_{t,wm}) \frac{du_{\parallel}}{dy} \right] = 0, \quad (2.1)$$

$$\frac{d}{dy} \left[ (\mu + \mu_{t,wm}) u_{\parallel} \frac{du_{\parallel}}{dy} + c_p \left( \frac{\mu}{Pr} + \frac{\mu_{t,wm}}{Pr_{t,wm}} \right) \frac{dT}{dy} \right] = 0, \quad (2.2)$$

where  $y$  and  $u_{\parallel}$  denote the wall-normal coordinate and the velocity component parallel to the wall, respectively.  $c_p$  and  $Pr$  denote the specific heat capacity at constant pressure and the molecular Prandtl number, respectively. The turbulent Prandtl number is set to be  $Pr_{t,wm} = 0.9$ .  $\mu_{t,wm}$  denotes the eddy viscosity given by a zero-equation mixing-length model as

$$\mu_{t,wm} = \kappa \rho y \sqrt{\frac{\tau_w}{\rho}} D, \quad (2.3)$$

where  $\kappa = 0.41$  is the von Kármán constant. In order to recover the linear behavior in the viscous sublayer, the damping function  $D$  is defined as

$$D = \left[ 1 - \exp \left( -\frac{y_{vD}^+}{A^+} \right) \right]^2, \quad (2.4)$$

where the dimensionless constant  $A^+ = 17$  indicates the characteristic length scale of the exponential damping.  $y_{vD}^+ = y/(\nu_w/u_{\tau})$ , where  $\nu_w$  and  $u_{\tau}$  denote the kinematic viscosity and friction velocity at the wall. However, Iyer & Malik (2019) and Yang (2017) show that the van Driest transformation performs poorly in collapsing the compressible velocity profile onto the incompressible counterpart for wall-bounded flows with cold isothermal condition. In this work, we use the semi-local scaling

$$y_{SL}^+ = \frac{\rho(y) \sqrt{(\tau_w/\rho)} y}{\mu(T(y))}, \quad (2.5)$$

where the dynamic viscosity is computed on the basis of the local conditions at an off-wall distance,  $y$ , and  $y_{SL}^+$  is used in place of  $y_{vD}^+$  in Eq. (2.4).

### 2.2. Numerical methods

In this work, the compressible, finite-volume code charLES (Bres *et al.* 2018) is used to conduct the numerical simulations herein. The numerical method consists of a low-

dissipation, approximate entropy-preserving scheme that deploys numerical dissipation around discontinuities. The LES governing equations are temporally integrated by the explicit third-order strong-stability-preserving (SSP) Runge-Kutta method (Gottlieb *et al.* 2001). The spatial and temporal schemes converge to second- and third-order with respect to the nominal mesh spacing and time step, respectively. Moreover, charLES is highly scalable and suitable for complex geometries by generating high-quality unstructured Voronoi meshes (Aurenhammer 1991). More comprehensive discussions and validations regarding the solver discretization and its capabilities can be found in Brès & Lele (2019), Lakebrink *et al.* (2019), Lozano-Durán *et al.* (2020), and Fu *et al.* (2020).

### 3. Double-finned problem definition and computational setup

The present geometry and computational setup follow those described in the experiment of a  $15^\circ$  double-finned configuration (Kussoy & Horstman 1992). The geometry is composed of two sharp fins with a wedge angle  $\alpha = 15^\circ$  fastened to a flat plate, as shown in Figure 1. Specifically, each fin is 20 cm high and 40.6 cm long, and the flat plate is 220 cm long and 10 cm high. The double fins are placed 165 cm downstream of the leading edge of the flat plate such that there is sufficient length for the turbulent boundary layer to develop. In terms of the flow configuration, the free-stream flow diagnosed at 3 cm ahead of the double fins (i.e., at  $x_o = 162$  cm) has a free-stream Mach number  $Ma_\infty = 8.23$  and Reynolds number  $Re_{\delta_o} = 1.7 \times 10^5$  based on the local boundary layer thickness  $\delta_o = 3.25$  cm. The wall is isothermal and cold with a temperature  $T_w = 300$  K, which is substantially lower than the stagnation temperature  $T_o = 1177$  K. Velocity, temperature, density and length are normalized by the sound speed  $c_r = 179$  m/s, the reference temperature  $T_r = 80$  K, the reference density  $\rho_r = 0.0186$  kg/m<sup>3</sup> and the reference length  $L_r = 1$  cm, respectively. The relation between the dynamic viscosity and the temperature is characterized by the Sutherland's law with a model constant  $S/T_r = 1.38$ . The calorically perfect gas assumption is adopted on the basis of the low free-stream temperature,  $T_\infty = 80$  K. For the governing equations of both the LES method and the wall model, the laminar and turbulent Prandtl numbers are set as  $Pr = 0.72$  and  $Pr_t = 0.9$ , respectively.

The computational geometry is given in Figure 2(a). The computational domain is sufficiently large such that there are no artificial reflections from the far-field outflow boundaries. The inlet flow condition is imposed by combining a uniform flow with the turbulence fluctuations generated by the synthetic turbulence generation method (Wu 2017). The computational domain is discretized with the  $7 \times 10^7$  Voronoi mesh elements adaptively clustering near the wall, as shown in Figure 2(b,c,d). The high mesh quality is guaranteed by the iterative smoothing operation based on the Lloyd's algorithm in charLES. On the basis of the resolution of the finest Voronoi mesh element near the wall, the turbulent boundary layer at  $x_o = 162$  cm is effectively resolved by approximately 40 cells (the present resolution is much coarser than that employed for studying the confinement effects in shock wave/turbulent boundary layer interactions; see Table 1 of Bermejo-Moreno *et al.* (2014)). However, as shown by Table 1, the total mesh element number inside the boundary layer is much less due to the coarsening in the wall-normal direction, as seen in Figure 2(d). It is infeasible to further coarsen the deployed grid for the following two reasons. Firstly, further coarsening the grid will lead to insufficient resolution to properly capture the boundary layer growth from the sharp leading edge. Secondly, the secondary separation on the plate is small, and this resolution is sufficient

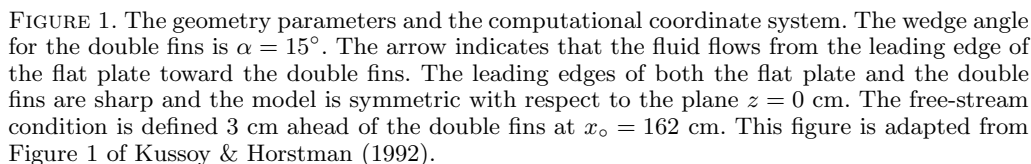


TABLE 1. Grid parameters inside the turbulent boundary layer upstream of the double fins.

Figure 3 shows the time-averaged  $y^+$  at the first off-wall cell centers, i.e., the matching locations for the wall model. The largest  $y^+$  appears around the leading edges of the double fins and the regions where the shock waves impinge on the surfaces. It is clear that the near-wall flow is not directly resolved in the simulations and that the wall model plays a pivotal role in the predicted flow states.

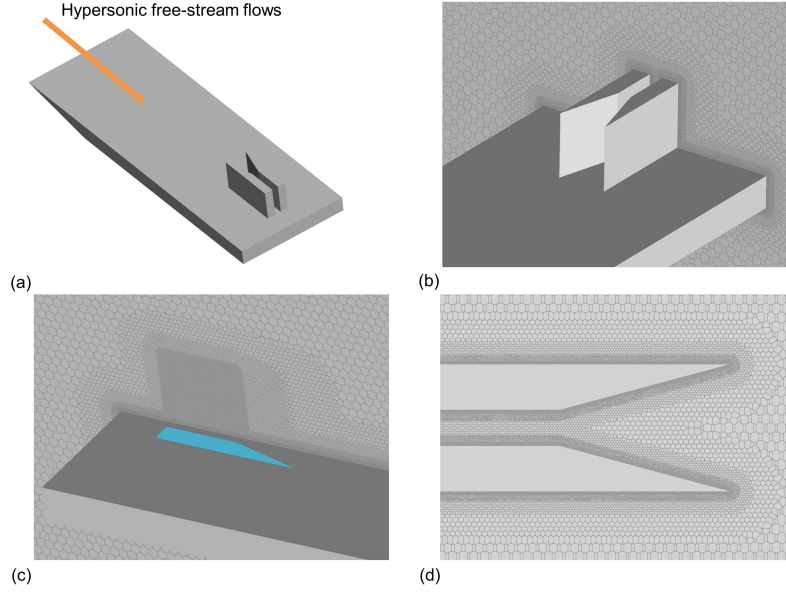


FIGURE 2. Computational geometry and mesh sketch for the double-fin simulations: (a) the overview of the computational geometry; (b,c,d) the zoomed-in views of the Voronoi mesh distributions. The grid includes 70 M Voronoi mesh elements in total.

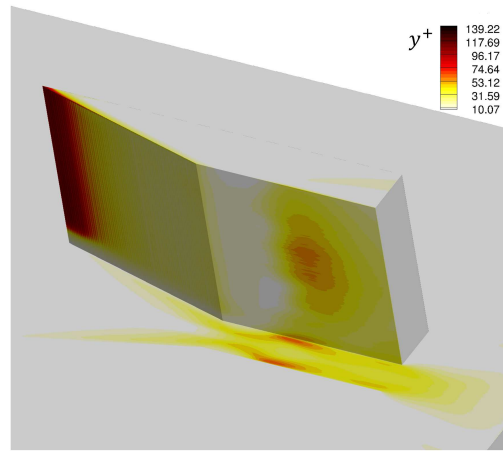


FIGURE 3. Distribution of the time-averaged  $y^+$  at the first off-wall cell centers. For facilitating the presentation, only the data over the flat plate and one vertical fin are shown.

#### 4. Numerical results

As shown in Figure 4, the flow evolves to the fully turbulent state ahead of the double-fin entrance. On the other hand, downstream the fin shoulders, the large-scale structures appear between the two fins in the vicinity of the flat plate.

##### 4.1. Data analysis in $x$ - $z$ and $x$ - $y$ planes

The time-averaged surface pressure and heat flux distributions along the centerline of the plate between the two fins as well as the double-shock intersection location based on the

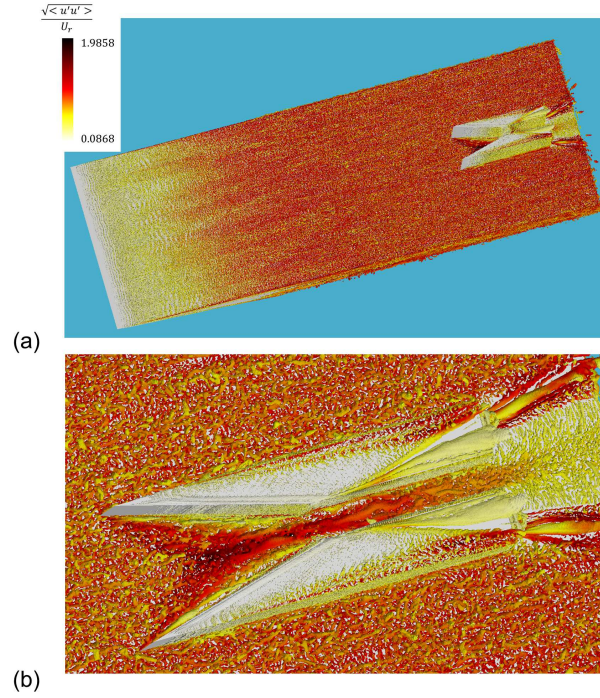


FIGURE 4. Instantaneous three-dimensional visualization of the isosurfaces of the second invariant  $Q$  of the velocity-gradient tensor colored by the magnitude of the dimensionless root-mean-square velocity. The value of  $Q$  on the isosurfaces is set to  $Q = 3.1c_r^2/L_r^2$ .

inviscid theory are given in Figure 5. The predicted time-averaged pressure distribution from WMLES, including the region downstream of the shock intersection, is in good agreement with the experiment. The static pressure first increases significantly due to the shock wave intersection and subsequently exhibits a rapid drop due to the expansions emanating from the fin shoulders, as depicted in Figure 6(a). In addition, the peak surface pressure  $\langle P_w \rangle / P_{w,\infty} \approx 22$  is considerably lower than the prediction from the inviscid theory,  $\langle P_w \rangle / P_{w,\infty} \approx 45$  (Gaitonde *et al.* 1995). Further downstream at  $x/L_r \approx 198$ , a smaller pressure peak appears due to the second crossing of the reflected shock waves. In terms of the heat flux distribution, the agreement with the experimental data is also favorable across the entire channel between the double fins. The streamwise variation of the surface heat flux follows that of the surface pressure qualitatively. In detail, both the experiment and the WMLES results exhibit an initial decline at  $x/L_r \approx 170$ , and the predicted heat flux is 20% smaller than that from the experiment in the pre-shock region of  $x/L_r \approx 180$ , which is the location of a secondary small-flow separation. Downstream of the shock wave intersection, the peak heat flux shows a 4% discrepancy between the WMLES results and the experimental data. Similar difference is also observed further downstream at  $x/L_r = 194$  in the low-pressure region and heat flux valley (see also Figure 6). Nevertheless, the present prediction of both quantities shows a much better agreement with the experiment than those from the RANS simulations (Narayanswami *et al.* 1993; Gaitonde *et al.* 1995). In the RANS solutions, the heat flux plateau around  $x/L_r = 180$  before the shock wave intersection is completely missed and great sensitivity is noticed with regard to the choice of length scale definition in the Baldwin-Lomax model

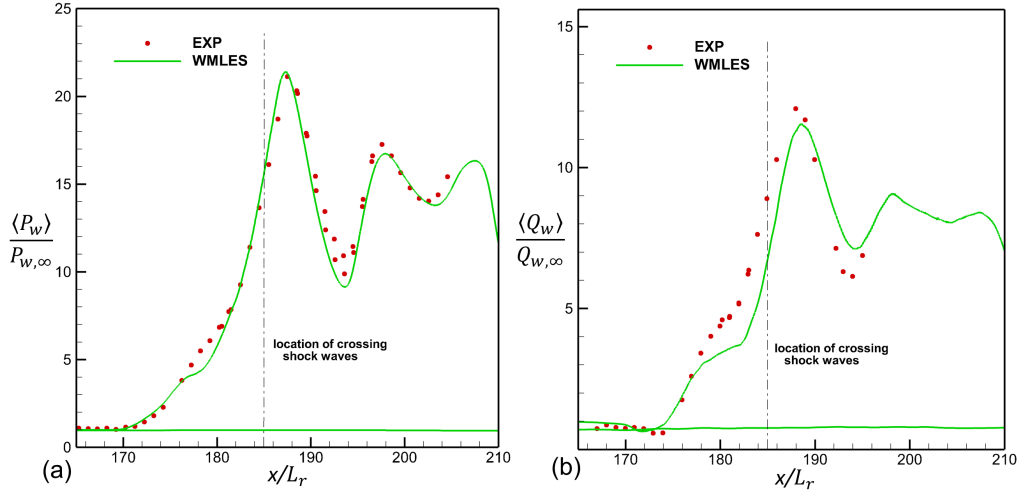


FIGURE 5. Streamwise distributions of the time-averaged (a) surface pressure and (b) surface heat flux on the flat plate at  $y/L_r = 0$  and  $z/L_r = 0$ . The lines and the dots denote the results from the WMLES simulation and the experiment, respectively. The location of the double-shock intersection based on the inviscid theory is also shown in the plots.

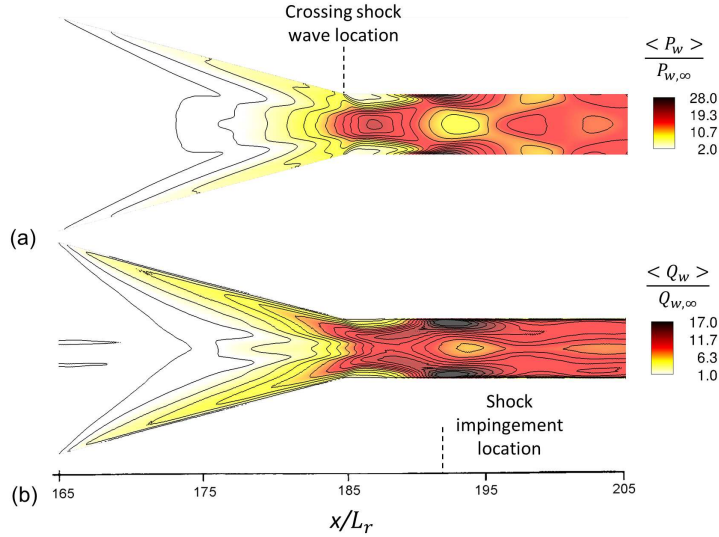


FIGURE 6. Distributions of the time-averaged (a) surface pressure and (b) surface heat flux on the flat plate at  $y/L_r = 0$ . The location of the double-shock intersection based on the inviscid theory is also shown in the plots. Also shown is the shock impingement location at around  $x/L_r = 192$ .

(see Figures 4 and 5 in Gaitonde *et al.* (1995)). Both the zero-equation Baldwin-Lomax model and the two-equation  $k - \epsilon$  model overpredict the peak pressure and the peak heat flux by about 20% (see Figures 3 and Figure 9 in Narayanswami *et al.* (1993)). As shown in Figure 6, the predicted location of the nominal shock impingement on the side fins is around  $x/L_r = 192$  and agrees well with that from the RANS method (see Figure 3 of Gaitonde *et al.* (1995)).

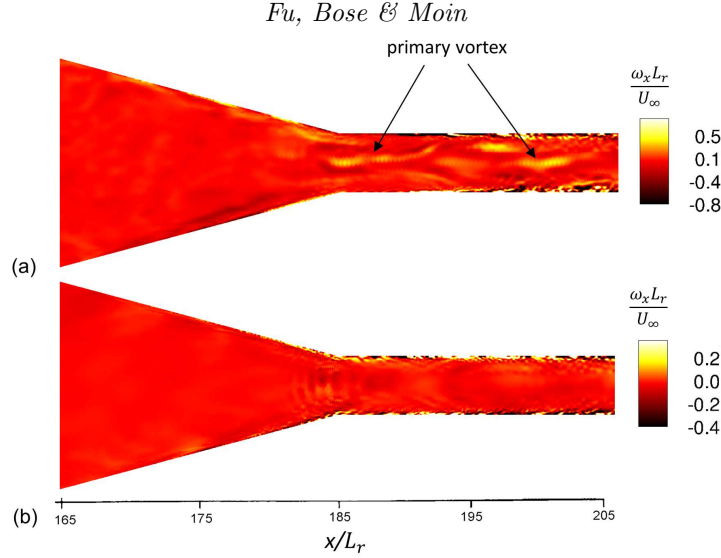


FIGURE 7. The distributions of the instantaneous streamwise vorticity on the wall-parallel  $x - z$  planes at (a)  $y/L_r = 2.5375$  and (b)  $y/L_r = 5.075$ .

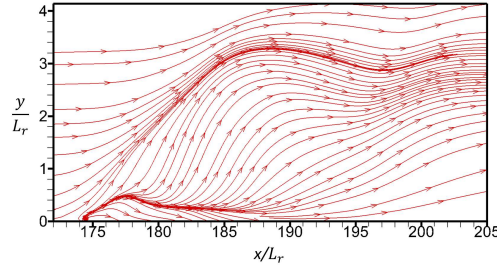


FIGURE 8. The zoomed-in view of the time-averaged streamlines on the symmetry plane. Around  $x/L_r \approx 174.5$ , there is a critical stagnation point located very close to the plate.

Concerning the boundary layer development on the side fins, the distributions of the instantaneous streamwise vorticity on the wall-parallel planes at  $y/L_r = 2.5375$  and  $5.075$  are visualized in Figure 7. The large-scale flow structures induced by the primary vortex can be identified from the streamwise vorticity distribution on the plane of  $y/L_r = 2.5375$ , whereas they are invisible on the further upward plane at  $y/L_r = 5.075$ , where the flow is out of the effect of the primary vortex. For both cases, the boundary layer is greatly excited downstream of the location of the nominal shock impingement on the side fins at around  $x/L_r = 192$ .

Figure 8 shows the zoomed-in view of the time-averaged streamlines on the symmetry plane. The maximum height of the secondary separation is roughly  $0.5$  cm at  $x/L_r \approx 178$ , which is much smaller than the inlet boundary layer thickness of  $3.25$  cm around the leading edge of the double fins, and the predicted flow structure is in accordance with that reported in Figure 11 of Gaitonde *et al.* (1995). This secondary separation bubble size is resolved with  $O(5)$  points across its height in the present case.



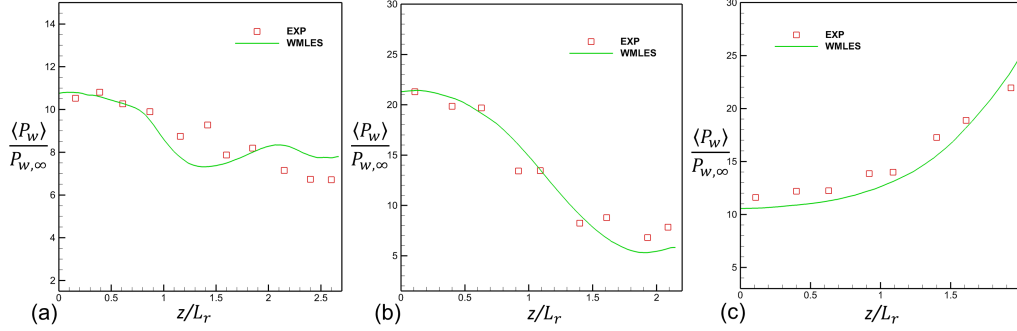


FIGURE 9. Spanwise distributions of the time-averaged wall pressure  $\langle P_w \rangle / P_{w,\infty}$  at the streamwise stations: (a)  $x/L_r = 183.2$ , (b) 187.5 and (c) 192. The experimental data (denoted as EXP) are adapted from the Table 4 of Kussoy & Horstman (1992).

#### 4.2. Data analysis in $y$ - $z$ planes

The spanwise distributions of the time-averaged surface pressure and surface heat flux at different streamwise stations are given in Figures 9 and 10, respectively. Considering the reported 10% uncertainties in the experimental data, the spanwise profiles of both quantities are well captured by the present WMLES simulation for all the considered streamwise stations. In terms of the time-averaged pressure profile, deviations from the experimental measurements are visible around the region with  $1.2 \leq z/L_r \leq 2.7$  at station  $x/L_r = 183.2$  before the shock intersection. The agreement becomes remarkably better at the two stations further downstream. On the other hand, the agreement of the heat flux distribution between the experimental data and the WMLES results is excellent for all three stations. The present results are also better than those from the RANS predictions with the zero-equation Baldwin-Lomax turbulence model (Gaitonde *et al.* 1995) and those from the two-equation  $k - \epsilon$  model (Narayanswami *et al.* 1993). As seen in Figure 6 of Gaitonde *et al.* (1995) and Figure 10(b), the spanwise heat flux distribution at  $x/L_r = 185.8$  is substantially overpredicted by the Baldwin-Lomax turbulence model. In Figure 10 of Narayanswami *et al.* (1993), it is concluded that both the zero-equation Baldwin-Lomax model and the two-equation  $k - \epsilon$  model perform poorly in terms of predicting the transverse profiles of flat plate surface heat transfer for all three streamwise stations.

### 5. Conclusions

In this study, the three-dimensional intersecting shock wave/turbulent boundary layer interaction flow over a double-fin geometry is investigated with the WMLES approach. The complex geometry with sharp edges and the high-Mach shock/boundary layer interaction with flow separation greatly challenge the mesh generation, the deployed numerics and the turbulence model. The comprehensive statistical comparisons between the WMLES results and the experimental data reveal that WMLES is capable of predicting the mean pressure and heat flux distributions accurately, in both the shock-impingement regime and the subsequent separation regime. Even the predicted flow structures in the secondary separation regions are in good agreement with the experimental measurement. The present result is better than those from RANS approaches based on the Baldwin-

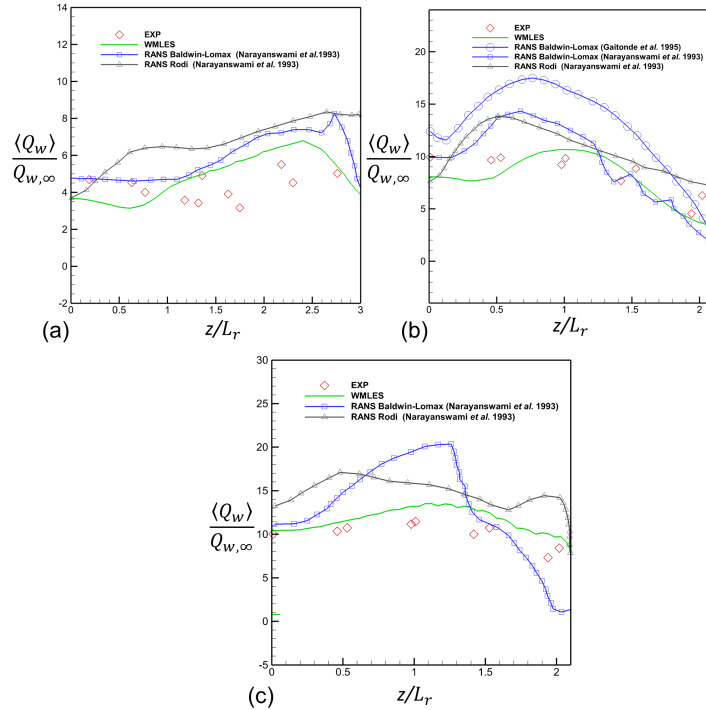


FIGURE 10. Spanwise distributions of the time-averaged wall heat flux  $\langle Q_w \rangle / Q_{w,\infty}$  at the streamwise stations: (a)  $x/L_r = 181.5$ , (b) 185.8 and (c) 190.3. The experimental data (denoted as EXP) are from the Table 4 of Kussoy & Horstman (1992). In panel (b), the RANS result is computed from the Baldwin-Lomax model with grid E - IB, which is elaborated in Figure 6 of Gaitonde *et al.* (1995). For all three panels, the RANS predictions in Narayanswami *et al.* (1993) with the zero-equation Baldwin-Lomax model and the two-equation  $k - \epsilon$  (Rodi) model are also shown for comparison. The locations of the spanwise measurements of the surface heat flux are not coincident with those of the surface pressure in Figure 9.

Lomax and the  $k - \epsilon$  models, in particular for the spanwise distributions of the surface heat flux.

## Acknowledgments

This work was funded by the US Air Force Office of Scientific Research (AFOSR) grant FA9550-16-1-0319. The authors acknowledge use of computational resources from the Yellowstone cluster in CTR. Mori Mani and Matthew Lakebrink from Boeing Research & Technology are greatly acknowledged for suggesting this case to the authors. The first author appreciates useful discussions with Kevin Griffin and Christopher Williams at CTR, Stanford University.

## REFERENCES

- ADAMS, N. A. 2000 Direct simulation of the turbulent boundary layer along a compression ramp at  $M=3$  and  $Re_\theta = 1685$ . *J. Fluid Mech.* **420**, 47–83.
- AURENHAMMER, F. 1991 Voronoi diagrams—a survey of a fundamental geometric data structure. *ACM Comput. Surv.* **23** (3), 345–405.

- BERMEJO-MORENO, I., CAMPO, L., LARSSON, J., BODART, J., HELMER, D. & EATON, J. K. 2014 Confinement effects in shock wave/turbulent boundary layer interactions through wall-modelled large-eddy simulations. *J. Fluid Mech.* **758**, 5–62.
- BOSE, S. T. & PARK, G. I. 2018 Wall-modeled large-eddy simulation for complex turbulent flows. *Annu. Rev. Fluid Mech.* **50**, 535–561.
- BRES, G. A., BOSE, S. T., EMORY, M., HAM, F. E., SCHMIDT, O. T., RIGAS, G. & COLONIUS, T. 2018 Large-eddy simulations of co-annular turbulent jet using a Voronoi-based mesh generation framework. In *2018 AIAA/CEAS Aeroacoustics Conference*, p. 3302.
- BRÈS, G. A. & LELE, S. K. 2019 Modelling of jet noise: a perspective from large-eddy simulations. *Philos. Trans. R. Soc. A* **377**, 20190081.
- CANDLER, G. V. 2019 Rate effects in hypersonic flows. *Annu. Rev. Fluid Mech.* **51**, 379–402.
- CHOI, H. & MOIN, P. 2012 Grid-point requirements for large eddy simulation: Chapman’s estimates revisited. *Phys. Fluids* **24** (1), 011702.
- DUAN, L., BEEKMAN, I. & MARTIN, M. P. 2011 Direct numerical simulation of hypersonic turbulent boundary layers. Part 3. Effect of Mach number. *J. Fluid Mech.* **672**, 245–267.
- FU, L., KARP, M., BOSE, S. T., MOIN, P., & URZAY, J. 2020 Shock-induced heating and transition to turbulence in a hypersonic boundary layer. *J. Fluid Mech.* **909**, A8.
- GAITONDE, D., SHANG, J. & VISBAL, M. 1995 Structure of a double-fin turbulent interaction at high speed. *AIAA J.* **33** (2), 193–200.
- GAITONDE, D. V. 2015 Progress in shock wave/boundary layer interactions. *Prog. Aerosp. Sci.* **72**, 80–99.
- GOTTLIEB, S., SHU, C.-W. & TADMOR, E. 2001 Strong stability-preserving high-order time discretization methods. *SIAM Rev.* **43** (1), 89–112.
- HADER, C. & FASEL, H. F. 2019 Direct numerical simulations of hypersonic boundary-layer transition for a flared cone: fundamental breakdown. *J. Fluid Mech.* **869**, 341–384.
- IYER, P. S. & MALIK, M. R. 2019 Analysis of the equilibrium wall model for high-speed turbulent flows. *Phys. Rev. Fluids* **4** (7), 074604.
- KUSSOY, M. & HORSTMAN, K. 1992 Intersecting shock-wave/turbulent boundary-layer interactions at Mach 8.3. *NASA Ames Research Center Technical Report, NASA-TM-103909*.
- LAKEBRINK, M. T., MANI, M., ROLFE, E. N., SPYROPOULOS, J. T., PHILIPS, D. A., BOSE, S. T. & MACE, J. L. 2019 Toward improved turbulence-modeling techniques for internal-flow applications. *AIAA Paper 2019-3703*.
- LARSSON, J., KAWAI, S., BODART, J. & BERMEJO-MORENO, I. 2016 Large eddy simulation with modeled wall-stress: recent progress and future directions. *Mech. Eng. Rev.* **3** (1), 15–00418.
- LEYVA, I. A. 2017 The relentless pursuit of hypersonic flight. *Phys. Today* **70**, 30–36.
- LOZANO-DURÁN, A., BOSE, S. T. & MOIN, P. 2020 Prediction of trailing edge separation on the NASA Juncture Flow using wall-modeled LES. *AIAA Paper 2020-1776*.
- NARAYANSWAMI, N., HORSTMAN, C. & KNIGHT, D. 1993 Numerical simulation of crossing shock/turbulent boundary layer interaction at Mach 8.3: comparison of zero and two-equation turbulence models. *AIAA Paper 93-0779*.

- SANDHAM, N., SCHÜLEIN, E., WAGNER, A., WILLEMS, S. & STEELANT, J. 2014 Transitional shock-wave/boundary-layer interactions in hypersonic flow. *J. Fluid Mech.* **752**, 349–382.
- SCHNEIDER, S. P. 2008 Development of hypersonic quiet tunnels. *J. Spacecr. Rockets* **45** (4), 641–664.
- SCHUELEIN, E. 2014 Effects of laminar-turbulent transition on the shock-wave/boundary-layer interaction. *AIAA Paper 2014-3332*.
- WILLEMS, S., GÜLHAN, A. & STEELANT, J. 2015 Experiments on the effect of laminar–turbulent transition on the SWBLI in H2K at Mach 6. *Exp. Fluids* **56** (3), 49.
- WU, X. 2017 Inflow turbulence generation methods. *Annu. Rev. Fluid Mech.* **49**, 23–49.
- YANG, X. I. A. 2017 On the eddy viscosity formulation in large-eddy simulation wall models. *Annual Research Briefs*, Center for Turbulence Research, Stanford University, pp. 271–283.